ORNL/LTR-2019/1104

Complete Status Report Documenting the Processing, Microstructure and High-Temperature Mechanical Properties of the Nano-structured Ferritic Alloy OFRAC

Nuclear Technology Research and Development

Prepared for
U.S. Department of Energy
Nuclear Technology R&D
Advanced Fuels Campaign

David T. Hoelzer, Rachel L. Seibert, Caleb P. Massey

Oak Ridge National Laboratory

June 30, 2019
M3NT-19OR020302051

ACKNOWLEDGMENTS

This research was sponsored by the U.S. Department of Energy, Office of Nuclear Energy, for the Nuclear Technology Research and Development (NTRD) program. The authors are grateful to Eric Manneschmidt (ORNL) for assistance with the strain-rate jump tests and to Anoop Kini and Baptiste Gault (Max-Planck-Institut für Eisenforschung GmbH, Düsseldorf, Germany) for assistance with the LEAP analysis of OFRAC specimens prepared from the extruded bar and annealed sample. The authors want to also acknowledge Arunodaya Bhattacharya and Daniel Morrall for reviewing the milestone report.

SUMMARY

This report provides a summary of the new nanostructured ferritic alloy, OFRAC (Oak Ridge Fast Reactor Advanced Fuel Cladding), that was developed for the advanced sodium fast reactor fuel cladding and core internals. The composition of OFRAC, which is Fe-12Cr-1Mo-03.Ti-0.3Nb + 0.3Y2O3 (wt. %), was chosen to achieve high temperature strength as well as high temperature creep performance and swelling resistance requirements that past structural materials such as austenitic stainless steels and ferritic/martensitic steels, i.e. HT-9, are not suitable as SFR cladding materials. The mechanical alloying procedures were described for producing OFRAC and the detailed characterization studies revealed uniformly distributed, high concentration of Y-Ti-O enriched oxide particles, or nanoclusters. The Nb addition that was intended to sequester interstitial C and N that are commonly introduced as contamination during ball milling of powder was found to be very effective in forming coarse size Nb carbonitrides along with excess Ti that removes these interstitial elements from the bcc-Fe matrix of OFRAC. The tensile tests on the OFRAC in the extruded condition showed excellent balance in strength and ductility from room temperature to 800ºC. Both the microstructure and tensile properties were not significantly degraded after annealing the extruded OFRAC samples for 8 h at 1050ºC and 1150ºC. The latter temperature is ~76% of the melting point of OFRAC. These results demonstrated the stability of the microstructure and tensile properties to extremely high temperatures. The thermal creep resistance at elevated temperatures and stresses was investigated using strain rate jump testing. The results showed that OFRAC possessed high stress exponents at high stresses and temperatures of 550ºC, 600ºC, 700ºC and 800ºC. This thermal dependence of minimum creep rate indicates that OFRAC will show quite low creep rates at higher temperatures and stresses compared to HT-9 and stainless steels. These significant improvements indicate that the NFA OFRAC alloy is a compelling and viable choice for sodium fast reactor fuel cladding.

CONTENTS

Page

FIGURES

FIGURES (CONTINUED)

TABLES

1. INTRODUCTION

Generation IV fission reactor concepts offer many benefits in economics, sustainability, reliability and safety compared to current Generation II water cooled fission reactors. The Generation IV reactors will also require structural materials for fuel cladding and core components that can tolerate high operating temperatures, applied stresses and neutron displacement damage levels. These requirements demand new high performance structural materials over structural materials that were predominately developed for current generation light water reactors as well as materials that were developed during the early research programs on liquid fast reactors during the 1970's and 1980's. Nanostructured ferritic alloys (NFA) are a class of advanced oxide dispersion strengthened (ODS) ferritic/martensitic (<12%Cr) and ferritic (>12%Cr) alloys that have the potential to deliver the desired high performance characteristics where historic austenitic stainless steels and ferritic/martensitic steels fall short.

Building upon the extensive research and development effort on the NFA 14YWT starting at ORNL in 2001, a new NFA referred to as OFRAC (Oak Ridge Fast Reactor Advanced Fuel Cladding), has been developed to address some of the challenges faced with 14YWT. The NFA 14YWT was developed for extreme neutron irradiation environments such as plasma facing components of fusion reactors and fuel cladding of fast fission reactors. The goals in development of 14YWT were to obtain ultra-fine grains plus a high concentration of nano-size Y-, Ti- and O-enriched nanoclusters (NC) for achieving high-strength and creep properties at elevated temperatures and providing high sink strength for trapping point defects to enhance recombination and for trapping transmutated He to form a high concentration of nano-size bubbles. Although most of these goals have been achieved with 14YWT, the new technological challenge is to fabricate complex components such as fuel cladding for fast reactor concepts. The NFA 14YWT contains 14%Cr, which means the bcc-Fe matrix is thermodynamically stable to the melting point of ~1510ºC. Thus, the processing and fabrication procedures for producing complex shaped components of 14YWT may result in the formation of microstructural textures that are detrimental to plastic deformation and cannot be easily modified by solid-state thermomechanical treatments except by recrystallization, which will compromise the salient microstructural features providing high temperature mechanical properties and radiation tolerance. The new NFA OFRAC is based on 12%Cr with additions of Mo, Ti, and yttria plus the addition of Nb for sequestration of impurity C and N within the microstructure. The 12%Cr level of OFRAC may also permit the partial transformation of bcc-ferrite to fcc-austenite at elevated temperatures that may be beneficial to changing the texture in the microstructure due to processing and fabrication.

Although not included in this report, the new NFA OFRAC was recently fabricated into a thin wall cladding geometry with a length > 1 m. A manuscript covering the OFRAC tube fabrication and characterization was submitted to the Journal of Nuclear Materials for publication [1]. The purpose of this milestone report is to document the processing, microstructure and high-temperature mechanical properties of OFRAC.

2. PROCESSING

2.1. Composition strategy

The composition of the nanostructured ferritic alloy (NFA) OFRAC is shown in Table 1. The 12%Cr (wt.%) addition was based on the development history of Cr-Mo steels that culminated in the HT9 steels for liqiud metal reactor core components [2]. According to the binary phase diagram (ASM International) shown in Figure 1, the 12%Cr (12.8 at.%) traverses the two-phase field between α-bcc (body centered cubic) ferrite phase and the γ-fcc (face centered cubic) austenite phase at ~910ºC up to ~1125ºC. Vertical lines are shown on the Fe-Cr phase diagram that illustrate the α-bcc + γ-fcc two phae region of OFRAC and the single

α-bcc phase region of 14WYT, which contains 14%Cr (14.8 at.%) for comparison. In future research and development of OFRAC, thermal-mechanical treatments will be conducted to investigate the effects of the α to γ phase reaction on the microstructure and mechanical properties.

The OFRAC alloy also includes solute additions of 1%Mo, 0.3%Ti and 0.3%Nb. The addition of Mo will contribute to solid solution strengtheing and favors the formation of $M_{23}C_6$ carbides and increases the start of the equilibriium transformation temperature from γ-fcc to α-bcc during cooling [3]. The role of the Nb addition is to sequester C and N from the α-bcc matrix to form MX-particles (FCC: $Fm\bar{3}m$ space group), where M = Nb and X = C, N [4,5]. Titanium can also react with C and N to form MX particles, however, the Nb-based MX particles are more resistant to high-temperature coarsening. The main purpose of adding Ti is to react with Y and O (from the Y_2O_3 dispersoid) to form the high concentration of nano-size Ti-Y-O oxide particles that are characteristic of NFA's such as 12YWT, MA957 and 14YWT [6,7]. For determining the concentration levels of Ti and Nb, calculations were based on the expected levels of O and C+N, respectively, increased during ball milling intentionally, i.e. O via Y_2O_3, and unintentionally as contamination, i.e. C from wear of components in the ball mill and O and N from the ingress of air.

Table 1. Composition of OFRAC, including the 0.3wt. % Y_2O_3 dispersoid addition.

Units	Fe	Cr	Mo	Ti	Nb	Y_2O_3
Wt. %	Bal.	12.00	1.00	0.30	0.30	0.30
At. %	Bal.	12.79	0.58	0.35	0.18	0.37

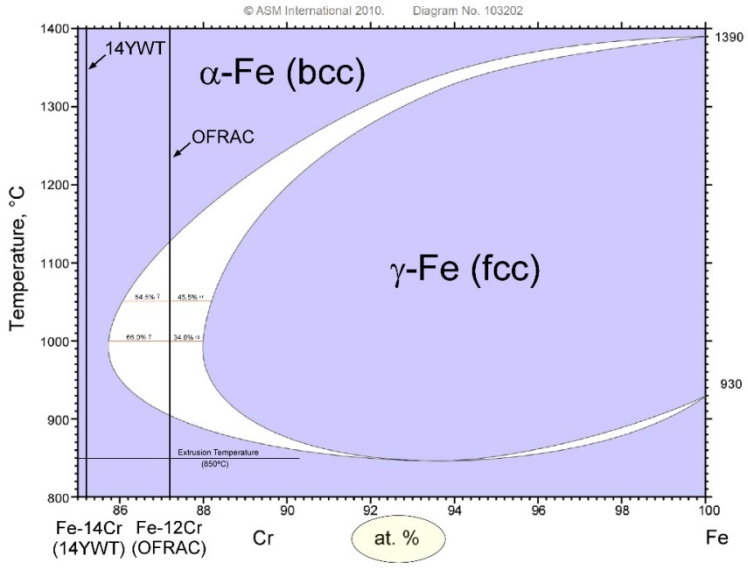

Figure 1. The Fe-Cr binary phase diagram of the Fe-rich side.

The powder of OFRAC was produced by ATI Powder Metals (PM) based on the nominal composition shown in Table 1. A total of 20 lbs. (9.072 kg) of powder was produced by Ar gas atomization with specifications for the solute additons of Cr, Mo, Ti and Nb and the acceptable limits of < 50 ppm for S and P, < 100 ppm for C, N, Al and Si and <200 ppm for O, Mn, Ni and all other non-alloying elements. The powder was sieved to -100/+325 mesh (-150/+45 μm) size range and shipped to ORNL. Table 2 shows the chemical analysis results of the atomized powder obtained by ATI PM. These results were acceptable by showing close agreement between the nominal composition and the atomized powder composition.

Table 2. Chemical analysis of the Ar gas atomized OFRAC powder (wt.%).

Fe	Cr	Mo	Ti	Nb	S	O	C	N
Bal.	**11.94**	**1.00**	**0.23**	**0.30**	**0.003**	**0.019**	**0.007**	**0.001**

2.2. Ball milling

The gas atomized OFRAC (Fe-12Cr-1.0Mo-0.3Ti-0.3Nb) powder was mixed with 0.3 wt.% Y_2O_3 powder that had a crystallite size range of 17-31 nm. The blended powder of 1 kg mass was ball milled using the high kinetic energy Zoz CM08 Simoloyer under Ar atmosphere for 40 h. Figure 2 shows the CM08 Simoloyer used for the ball milling runs. The ball milling run was conducted using 5 mm diameter low carbon steel milling media with a ball-to-powder ratio of 10:1.

Figure 2. The high kinetic energy Zoz CM08 Simoloyer.

2.3. Extrusion

The procedure for extruding the ball milled powder of OFRAC consisted of fabricating a can for holding the ball milled powder, degassing the can packed with powder and hot extrusion. The can was fabricated from mild steel and had a dimension of 3.9 in. diameter and 5.5 in. long. A lid to the can with a 0.25 in. (6.35 mm) diameter opening at the center was fabricated from mild steel. The ball milled powder was packed in the can and the lid was welded to the can. A 0.25 in. diameter stainless steel tube with fixture for connecting to the vacuum system was welded to the lid. The can was degassed under vacuum for 24 h at 300ºC. The stainless steel tube was crimped following the vacuum degassing. Figure 3 shows the components of the can (Fig. 3a) and several cans that have been packed with ball milled powder and vacuum degassed (Fig. 3b).

(a) (b)

Figure 3. Images showing (a) the 3.9 in. diameter x 5.5. in. long can and lid (a solid plug is also shown) fabricated from mild steel and (b) five cans packed with ball milled powder that were vacuum degassed after which the 0.25 in. diameter stainless steel tube was crimped.

The degassed can was extruded with the Watson-Stillman press, which has a capacity of 1,250 tons (~1.13 x 10^6 kg) and can accommodate cans up to 5.5 in. (~14 cm) diameter. The can was heated to 850ºC for 1 h in an open air furnace followed by extrusion through a rectangular shaped die that had an opening of 2.5 in. (6.35 cm) wide x 1.25 in. (3.175 cm) high. Figure 4 shows the extrusion press (Fig. 4a) and the extruded bar of OFRAC (Fig. 4b).

(a) (b)

Figure 4. Images showing (a) the Watson-Stillman extrusion press and (b) the rectangular shaped bar of OFRAC after extrusion.

Chemical analysis of the extruded OFRAC bar was performed by the company DIRATS using a combination of inductively coupled plasma optical emission spectroscopy (ICP-OES) and combustion analysis. Table 3 shows the chemical analysis results obtained by DIRATS in both weight percent. By comparing the composition of the extruded bar (Table 3) with that of the atomized powder (Table 2), the results indicate that the increase in O and N levels of ~0.0125% and ~0.0184%, respectively, were much lower than that of C (0.0370%) during ball milling. The higher O content is primarily due to the addition of 0.3% Y_2O_3, which contributed to 0.0640% (all % in wt.%). The C contamination is primarily from the wear of the rotor blade and ball media during 40 h of ball milling. However, the ball milling conditions that were used resulted in very little contamination by air entering the milling chamber.

Table 3. Chemical analysis of the extruded OFRAC bar (wt.%).

Fe	Cr	Mo	Ti	Nb	Y	S	O	C	N
Bal.	**12.25**	**0.89**	**0.20**	**0.27**	**0.22**	**0.0040**	**0.0955**	**0.0440**	**0.01850**

2.4. Annealing

Samples of the extruded OFRAC bar were fabricated for conducting annealing experiments to investigate the stability of the microstructure and tensile properties. The samples were annealed in a furnace capable of high vacuum (<10^{-6} Torr) for 8 h at 1050ºC and 1150ºC.

3. MICROSTRUCTURE

Specimens of the extruded OFRAC bar and the two annealed OFRAC samples were prepared for microstructrure analysis that included scanning electron microscopy (SEM), scanning/transmission electron

microscopy (S/TEM) and atom probe tomography (APT). For SEM analysis, the specimens were polished by metoallographic procedues with a final colloidal silica (0.05 μm) polish. Specimens for S/TEM and APT analysis were prepared using the focused ion beam (FIB) lift-out technique. This was performed using a FEI Quanta 3D dual-beam FIB to produce a lamellae specimen for S/TEM analysis and a sharp tip for APT analysis. The TEM lamella was cleaned using a Fischione Nanomill 1040 prior to S/TEM examination and a final sharpening of the APT tip was done using a FEI Helios 600 prior to APR analysis. The source was Ga ions for the FIB lift-out specimen preparations.

The polished specimens were examined in a Hitachi 4800 field emission (FE) SEM equipped with X-ray energy dispersive spectroscopy (XEDS). Back-scattered electron (BSE) images of the microstructure were obtained to show the grain size and morphology. The texture of the polished specimens was obtained by electron back scattered diffraction (EBSD) using a JEOL 6500F FESEM operating at 20 kV accelerating voltage with a 4 nA current and step size of 0.03 μm. The TEM lamella was examined using the FEI Talos F200X S/TEM quipped with the four silicon-drift-detectors (SDD) SuperX XEDS detector capable of high resolution imaging and composition mapping. The S/TEM imaging and XEDS composition mapping were performed with an accelerating voltage of 200 kV. The APT tip was analyzed on either a CAMECA Local electrode atom probed (LEAP) 4000X HR or a CAMECA LEAP 5000XR, which possessed dectection efficiencies of 36% and 52%, respectively. Details of the operating perameters used in the APT analysis have been recently published [8].

3.1 As-extruded

The grain structure of the extruded OFRAC bar that was observed by SEM-BSE imaging is shown in Figures 5 and 6. Both the longitudinal-LT (Fig. 5a and 6a) and transverse-TS (Fig. 5b and 6b) orientations are shown in the figures. The extrusion direction is parallel to the micrographs for LT and normal to the micrographs for TS. The BSE micrographs shown in Figure 5 were obtained at low magnification to show the apparent heterogeneity in the grain size and spatial distribution. Regions of the microstructure for both orientations consisted of small grains and coarse grains. This is most noticeable for the TS orientation observed in Figure 5b. The BSE migrographs observed in Figure 6 were obtained at higher magnification to reveal the size and morphology of grains contained in the small grain region. The yellow arrow and dot shown in the BSE micrographs in Figure 6 denote the extrusion directions. The grain anisotropy caused by extrusion is best observed in the LT orientation (Fig. 6a). However, the results indicate the grains are nearly

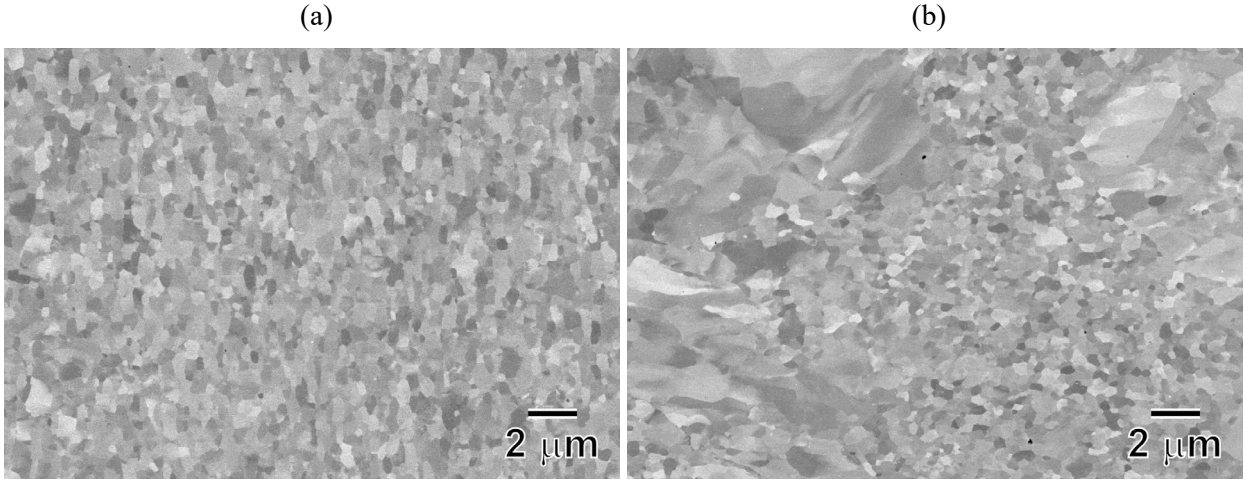

Figure 5. SEM-BSE micrographs obtained at low magnication of the microstructure present in the extruded OFRAC alloy in (a) the longitudinal-LT orientation and (b) the transverse-TS orientation.

equiaxed with a very small grain aspect ratio, r = length/width of the grains. This was determined by measuring the grain size in the LT orientation using the line intercept method in both the direction parallel and normal to the extrusion direction. The distribution of grain sizes in LT and TS orientations are shown in Figure 7. There is a small population of larger size grains measured in the parallel (major axis) direction compared to the normal (minor axis), but most of the grain sizes are distrubuted in the smaller size grains in the LT orientation. The average grain size was 570 +/- 260 nm and 490 +/- 210 nm for the LT and TS orientations, respectively.

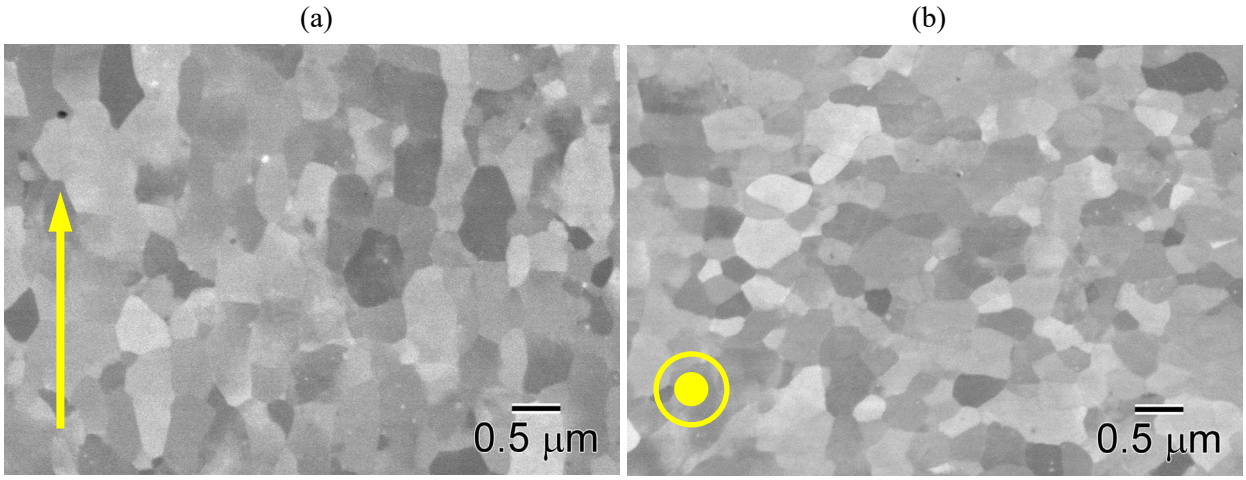

Figure 6. SEM-BSE micrographs obtained at higher magnification of the microstructure present in the extruded OFRAC alloy in (a) the longitudinal-LT orientation and (b) the transverse-TS orientation. The yellow arrow and dot represent the extrusion direction.

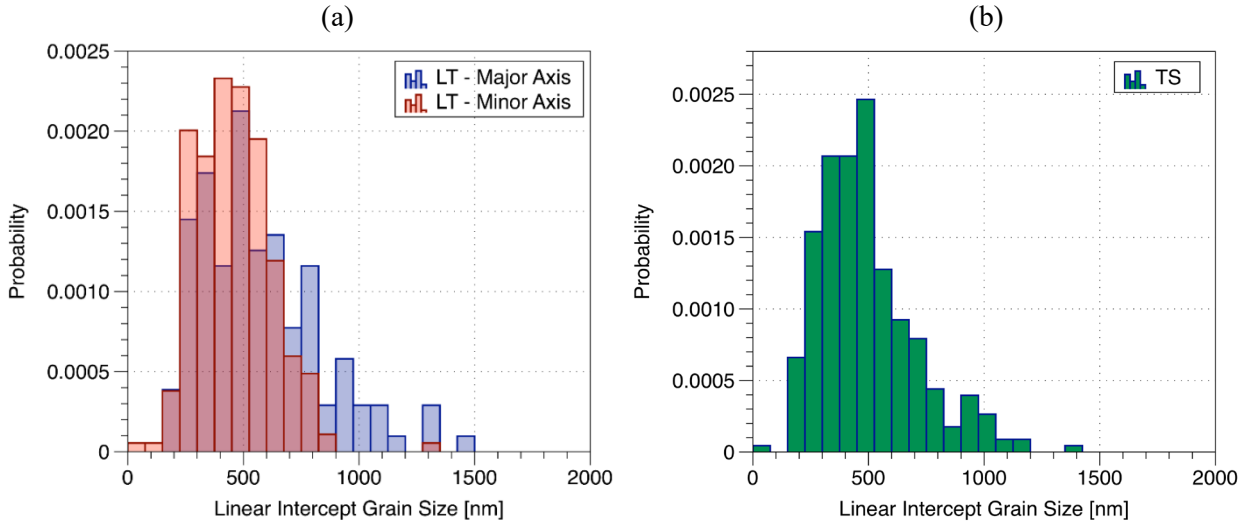

Figure 7. SEM-BSE micrographs of the microstructure observed at higher magnification in the (a) longitudinal-LT orientation and (b) transverse-TS orientation. The yellow arrow and dot represent the extrusion direction.

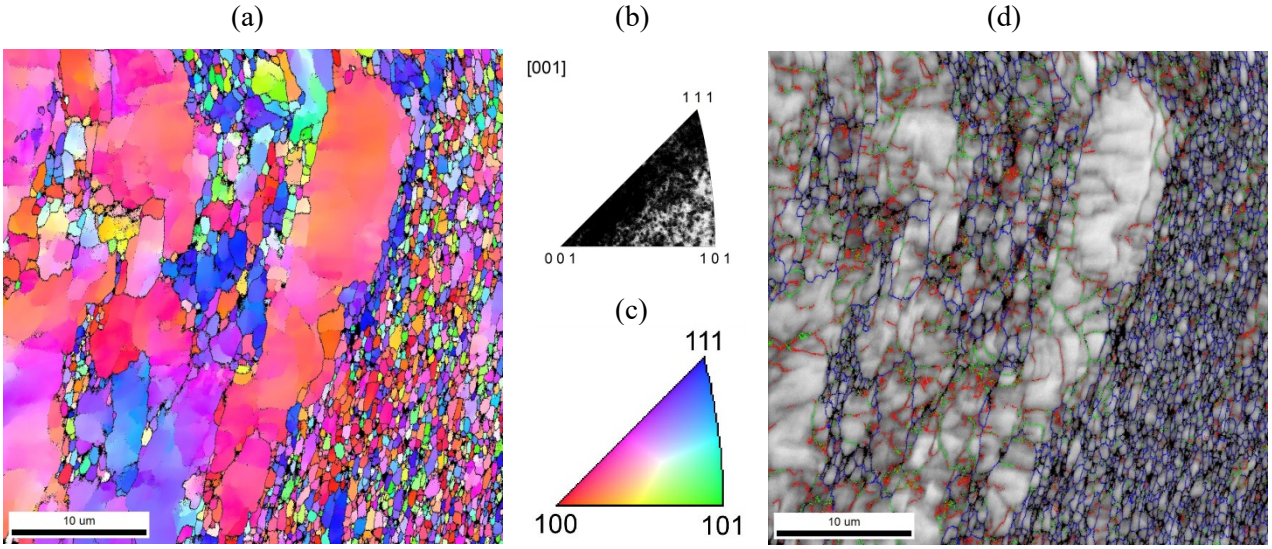

Figure 8. (a) EBSD pole figure map in the LT orientation, (b) inverse pole figure of the grains in the [001] normal direction, (c) the color triangle associated with the orientation of the grains observed in the EBSD pole figure map and (d) the grain boundary map showing the misorientaion angles between the grains.

The fine grain structure of the microstructure present in the extruded OFRAC bar observed by Bright-Field (BF) S/TEM analysis is shown in Figure 9. The microstucture consisted of a high dislocation density and dislocation networks that were associated with low angle subgrain boundaries within the grains. At higher magnication (Fig. 9b), a low number density of coarse size particles are present. A few of these particles are highlighted with yellow arrows in the micrograph. Element maps obtained by XEDS spectrum imaging in S/TEM mode of the microstructure are shown in Figure 10. The grain structure of the area that was analyzed is shown with the Dark Field (DF) S/TEM micrograph (Fig. 10a). It is difficult to observe the

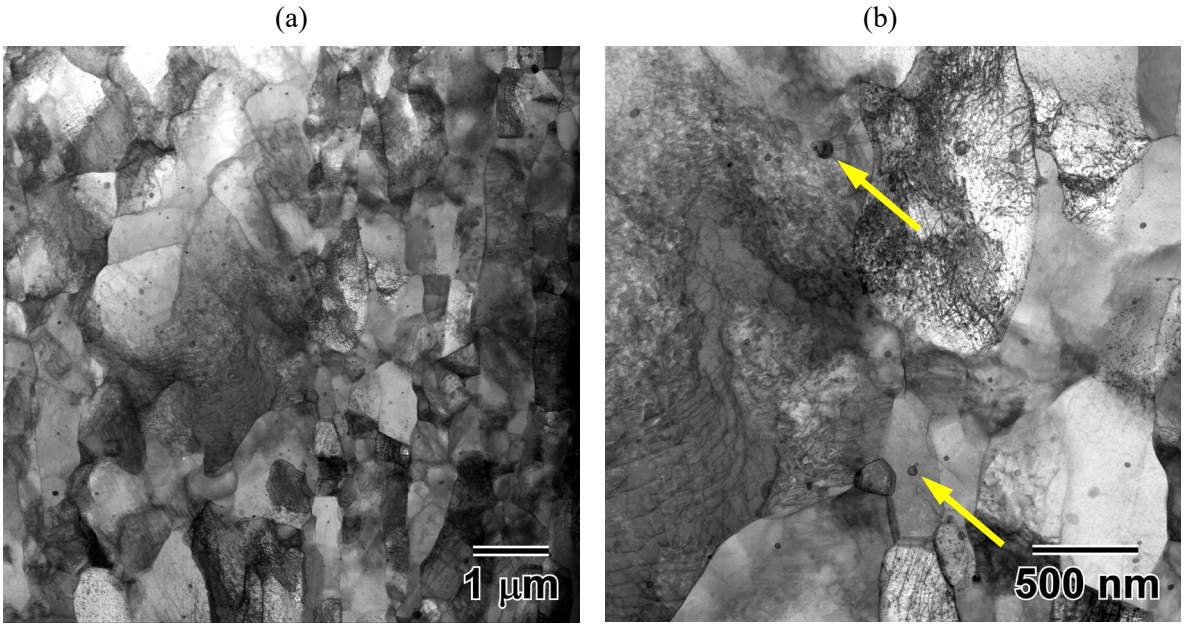

Figure 9. BF S/TEM micrographs showing the microstructure of the extruded OFRAC specimen at (a) low magnication and (b) high magnification with arrows highlighting coarse size particles.

coarse size particles by DF S/TEM. However, the Fe map (Fig. 10d) revealed numerous particles of varying sizes showing dark contrast due to depletion of Fe associated with the particles. Both Nb (Fig. 10b) and Ti (Fig. 10c) were found to be associated with these particles. The superpositioning of the Nb (blue) and Ti (yellow) maps (Fig. 10f) confirmed that both elements are present in the coarse size particles as determined by the color combination of blue and yellow resulting in the green color. Although noisy, the C map (Fig. 10e) also showed C enrichment with the Nb-Ti enriched particles. These results indicated that Nb and Ti are effective in gettering C, and N (not shown), in the matrix. The N maps were even noiser than the C map since the chemical analysis in Table 2 results showed higher C concentration (440 wpppm) compared to N (185 wpppm) in the extruded OFRAC bar. The crystal structure of the (Nb,Ti)C particles was analyzed by electron diffraction due in part to their relatively small size, however, these particles most likely are the MX carbo-nitrides. Future research will attempt to confirm the crystal structure of the (Nb,Ti)C using selected area (SAED) and convergent beam electron (CBED) diffraction techniques.

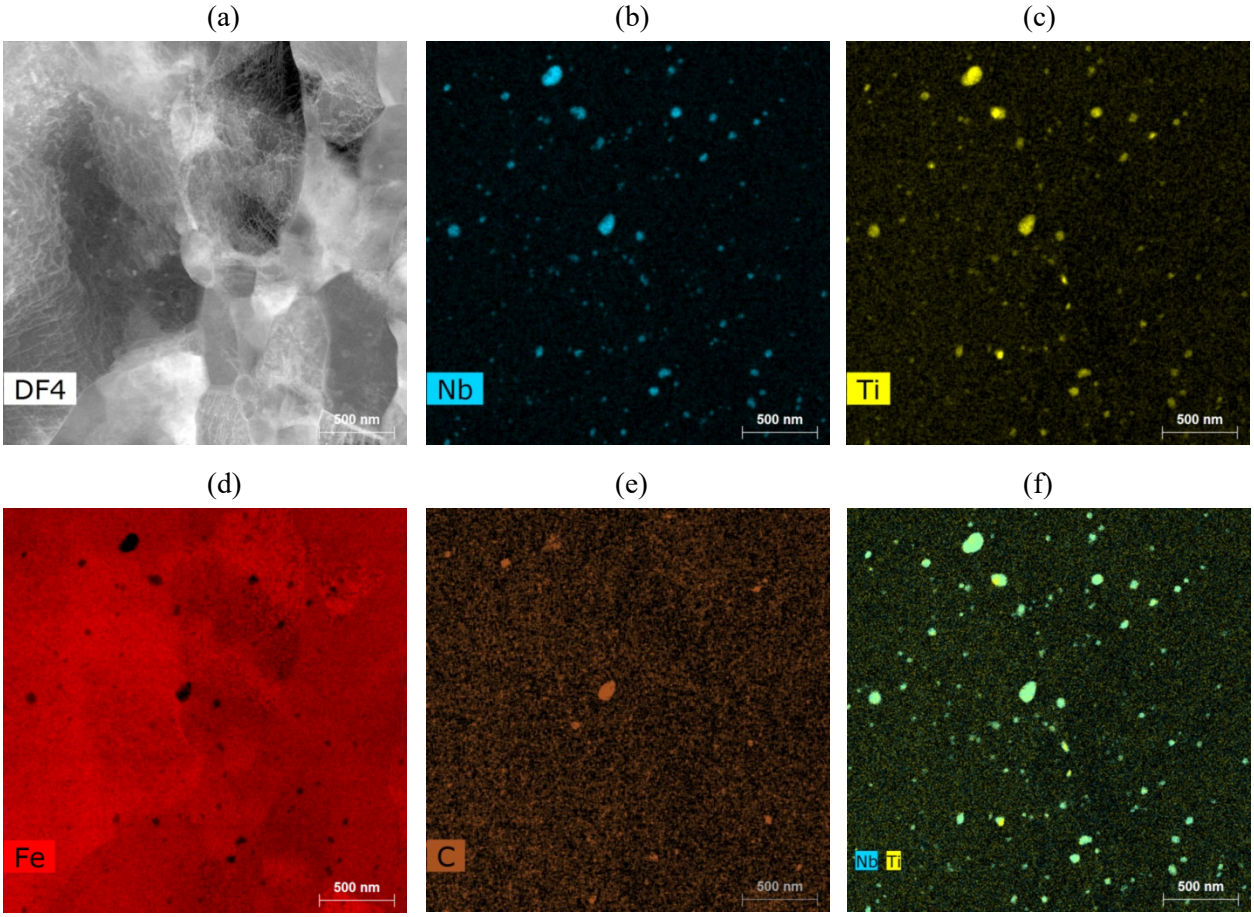

Figure 10. Element maps obtained by spectrum imaging in S/TEM mode of the microstructure present in the extruded OFRAC bar. (a) Dark Field S/TEM micrograph, (b) Nb map, (c) Ti map, (d) Fe map, (e) C map and (f) overlay of Nb and Ti maps.

The results of the LEAP anaysis of 6 specimens prepared from the extruded OFRAC bar are shown in Figure 11. The results revealed a high concentration of uniformly distributed Ti-Y-O enriched nano-size oxide (nanoclusters) particles in all the specimens. The reconstructed element map of one analyzed specimen (Fig. 11a) shows 1.5 at.% (Y,TiO) isoconcentration surfaces (green particles) associated with the nanoclusters combined with the 0.1 at.% Fe atom map of the matrix. The average diameter and number

density of the Ti-Y-O enriched nanoclusters obtained from analysis of 1871 clusters was 2.19 +/- 0.02 nm and 6.8×10^{23} +/- 0.66×10^{23} m^{-3}, respectively [8]. The composition correlated with the size of the analyzed nanoclusters is shown in the Y-Ti-O ternary diagram (Fig. 11b). The size of the analyzed nanocluster is shown by the diameter of the circle in this figure. The results show a composition range that varies with Ti, Y and O with no clear size correlation. However, the range in compositions for the nanoclusters do not correspond to equilibrium oxides in the Y-Ti-O ternary diagram, such as Y_2TiO_5 and $Y_2Ti_2O_7$. Table 4 shows the global composition obtained from the entire volume of the 6 APT specimens and the average nanocluster composition obtained using the chemical composition correction (CCC) model that corrects the erroneous artefact consisting of high Fe and Cr counts measured from the small nanoclusters in OFRAC. A thorough discussion of the challenges in determining the composition of nanoclusters by APT including the CCC model is provided in the recent publication by C.P. Massey et al. [8].

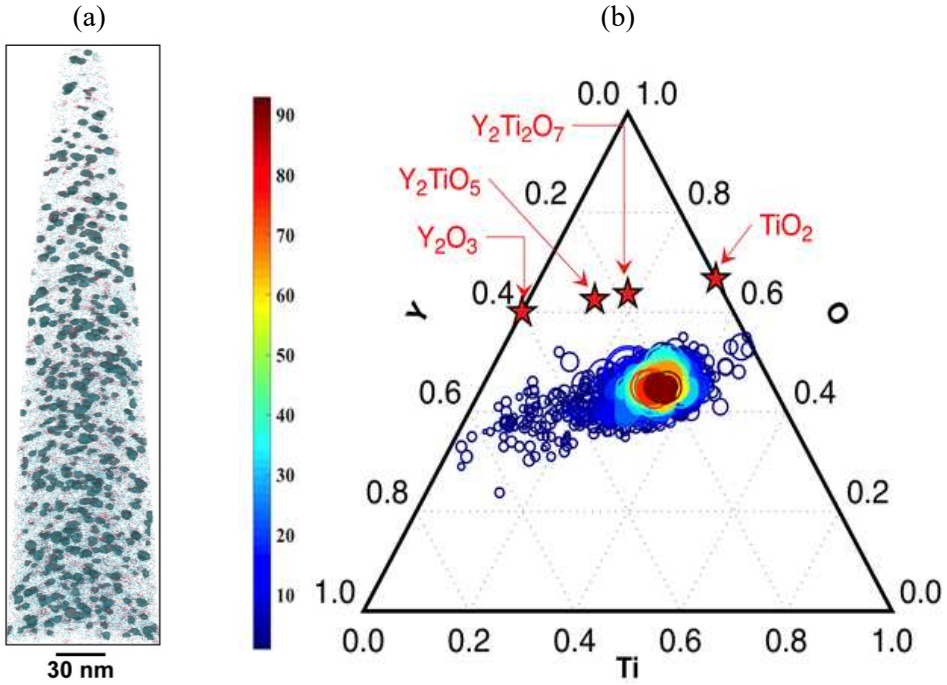

Figure 11. LEAP analysis of the specimen prepared from the extruded OFRAC bar. (a) the 1.5 at.% (Y,TiO) isoconcentration surfaces (green) associated with the nanoclusters combined with the 0.1 at.% Fe atom map of the matrix and (b) Y-Ti-O ternnary diagram showing the composition and size (circle diameter) of the analyzed nanoclusters.

3.2 Annealing for 8 h at 1050ºC

The SEM analysis of the OFRAC alloy after annealing for 8 h at 1050ºC is shown in Figures 12 and 13. The BSE microgrpahs show the LT (Fig. 12a and 13a) and TS (Fig. 12b and 13b) orientations. The BSE micrographs obtained at low magnification (Fig. 12) show the heterogeneity in the grain size and spatial distribution. The BSE migrographs obtained at higher magnification (Fig. 13) reveal the size and morphology of grains located in the small grain regions. The grains appear with some shape anisotropy, but still retained a small grain aspect ratio in both orientations. An unidentified phase formed during annealing that was observed by BSE imaging as large particles showing bright contrast, which are pointed with the yellow arrows in Figure 13. The bright contrast indicates the particles contain high atomic number (Z) elements such as Mo and Nb. The texture of the grain structure determined by EBSD in the LT orientation is shown in Figure 14. The EBSD pole figure map (Fig. 14a) shows the heterogeneity in grain size and

Table 4. The average global composition of the matrix and the average composition of the nanoclusters.

Element	Composition (at.%)	
	Global	Clusters*
Fe	85.49 ± 0.18	00.00 ± 00.00
Cr	13.05 ± 0.09	4.17 ± 0.14
Mo	0.50 ± 0.02	0.58 ± 0.03
Ti	0.16 ± 0.01	29.62 ± 0.14
Y	0.09 ± 0.01	23.18 ± 0.18
O	0.36 ± 0.10	40.51 ± 0.09
C	0.10 ± 0.06	0.46 ± 0.02
N	0.00 ± 0.00	0.01 ± 0.00

*Chemical composition correction (CCC) model [8].

spatial distribution. The correlated inverse pole figure (Fig. 14b) and calibrated color triangle (Fig. 14c) indicate that the normal direction of many grains was spread out over the orientations between the 100, 110 and 111 directions, suggesting a weaker 110 α-fiber texture compared to the extruded OFRAC alloy (Fig. 8). The coarse grains observed in the EBSD pole figure map show subtle variations in color that is indicative of sub-grain structures. The sub-grains associated with the coarse grains are consistent with the grain boundary map that correspond to grain misorientations measuring <15º (Fig. 14d). The regions consisting of the small grains are associated with much larger grain misorientation angles. The average grain diameter determined from grain area measurements using the EBSD software was 240 +/- 380 nm. The large standard deviation relative to the average grain size does not accurately account for the grain size. Most likely it was due to some grain coarsening during the annealing and the existence of a bimodal grain structure. However, the results indicate that despite the possible coarsening of grains, the grain coarsening was not signicant after annealing for 8 h at 1050ºC compared to the grain size observed in the extruded OFRAC alloy condition.

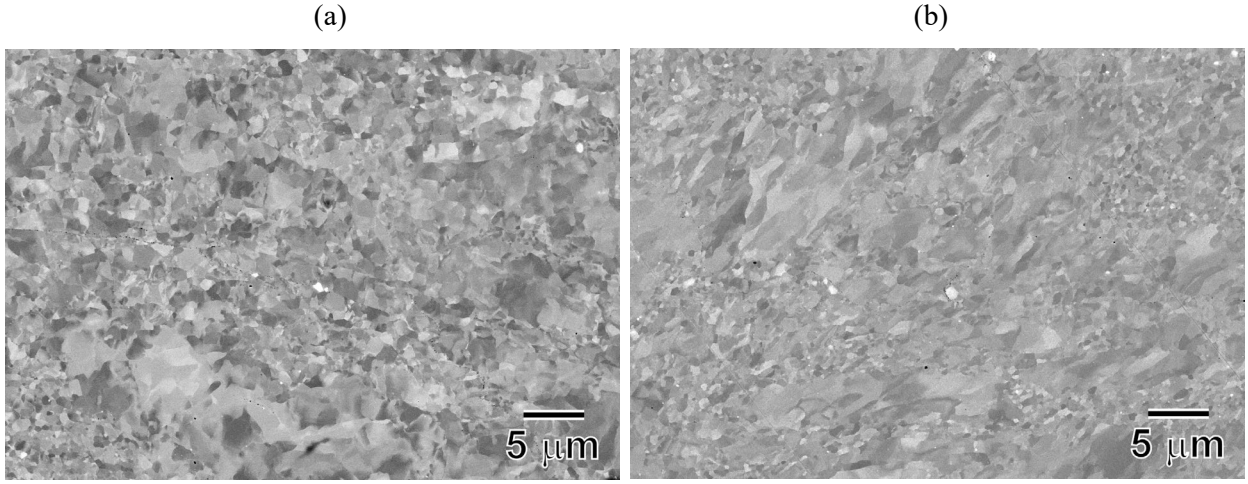

Figure 12. SEM-BSE micrographs obtained at low magnification of the microstructure present in the OFRAC alloy after annealing at 1050ºC for 8 h in (a) the LT orientation and (b) the TS orientation.

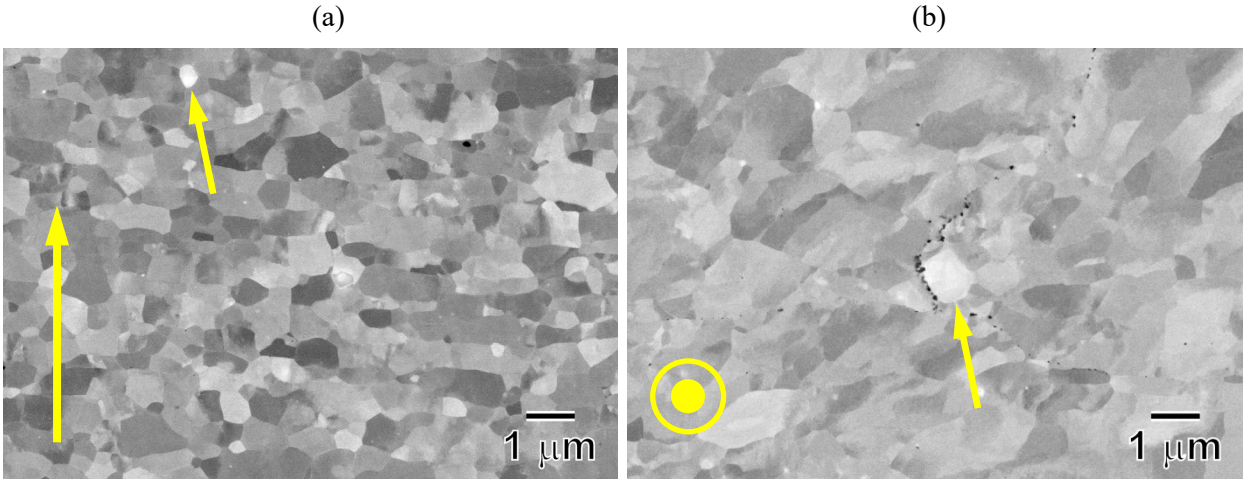

Figure 13. SEM-BSE micrographs obtained at higher magnification of the microstructure present in the OFRAC alloy after annealing at 1050ºC for 8 h in the (a) LT orientation and (b) TS orientation. The yellow arrow and dot represent the extrusion direction.

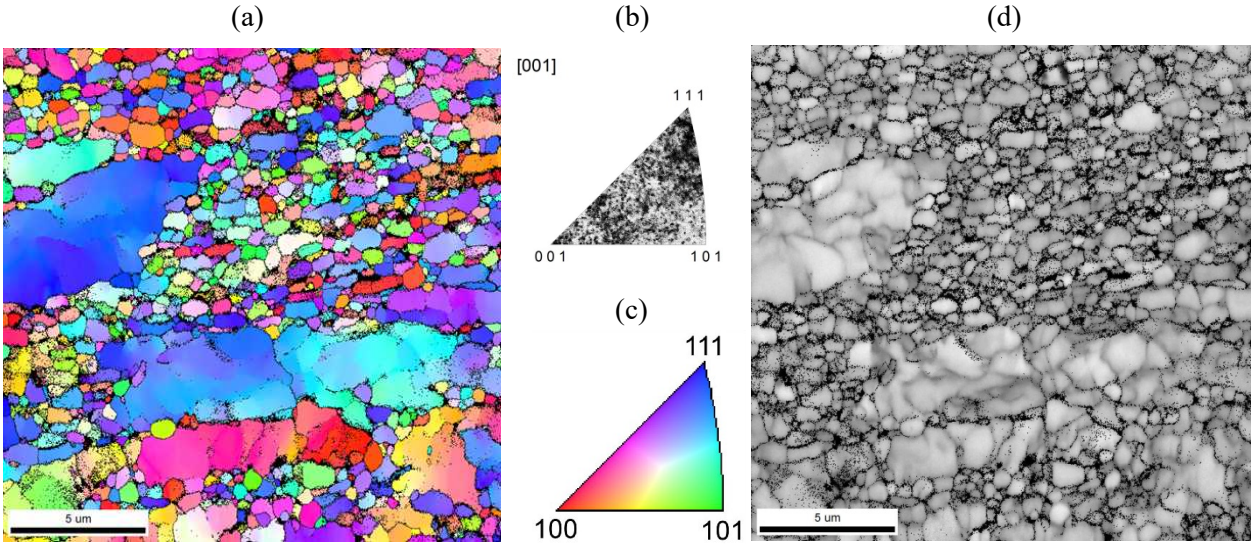

Figure 14. (a) EBSD pole figure map of the annealed 1050ºC/8 h OFRAC alloy in the LT orientation, (b) inverse pole figure of the grains in the [001] normal direction, (c) the color triangle associated with the orientation of the grains observed in the EBSD pole figure map and (d) the grain boundary map showing the misorientation angles between the grains.

3.3 Annealing for 8 h at 1150ºC

The SEM analysis of the OFRAC alloy after annealing for 8 h at 1150ºC is shown in Figures 15 and 16. This temperature is ~75% of the melting point for the OFRAC alloy, which represents a severe test of the microstructural stability of OFRAC. The BSE micrographs show the LT (Fig. 15a and 16a) and TS (Fig. 15b and 16b) orientations. The BSE micrographs obtained at low magnification (Fig. 15) show the heterogeneity in the grain size and spatial distribution. The BSE migrographs obtained at higher magnification (Fig. 16) reveal the size and morphology of grains located in the small grain regions. The grains show some anisotropy in shape, but still retained a small grain aspect ratio, r = length/width of the

grains in both orientations. The unidentified particle showing bright contrast in the BSE micrographs that was observed after annealing for 8 h at 1050ºC was also observed after annealing for 8 h at 1150ºC. However, these particles appeared to have coarsened at the higher annealing temperature. The particle observed by the yellow arrow in the LT orienation (Fig. 16a) appears larger than those observed at 1050ºC annealing (Fig. 13). The bright contrast of these particles indicates that the phase consists of elements with high atomic number (Z) such as Mo and Nb. Futher TEM analysis will be conducted to identify this unknow phase that forms in OFRAC during high temperature annealing. The texture of the grain structure determined by EBSD in the LT orientation is shown in Figure 17. The EBSD pole figure map (Fig. 17a) shows that the heterogeneity in grain size and spatial distribution increased with the 1150ºC annealing. The correlated inverse pole figure (Fig. 17b) and calibrated color triangle (Fig. 17c) indicate that the normal direction of many grains was spread out over the orientations between the 100 and 111 directions, which suggests that the 110 α-fiber texture was stronger compared to that observed in the annealed 1050ºC/8h OFRAC alloy (Fig. 14). The coarse grains observed in the EBSD pole figure map show the same type of subtle variations in color consistent with sub-grain structures, which is confirmed with the grain boundary

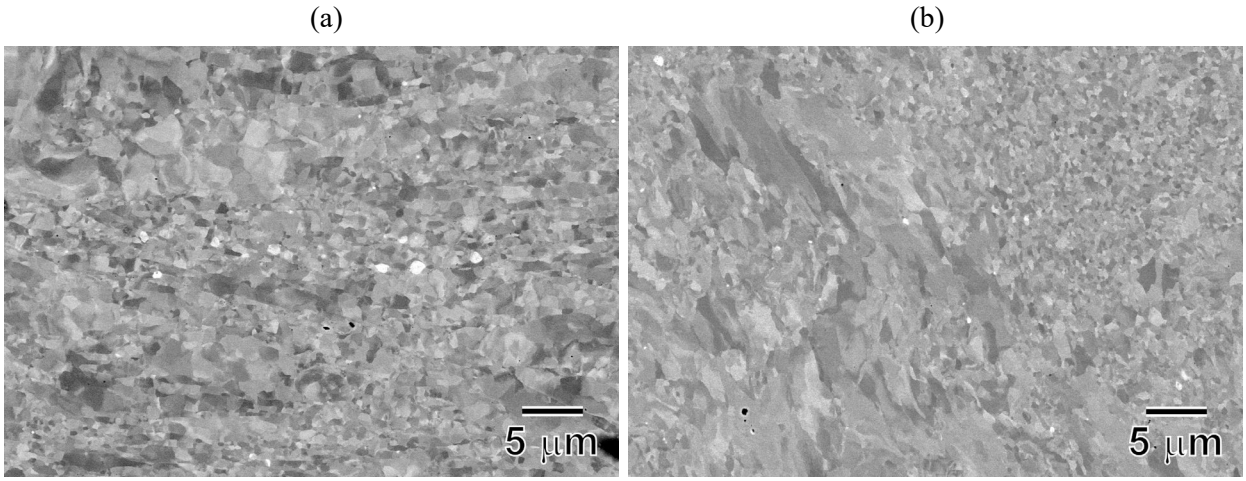

Figure 15. SEM-BSE micrographs obtained at low magnification of the microstructure present in the OFRAC alloy after annealing at 1150ºC for 8 h in (a) the LT orientation and (b) the TS orientation.

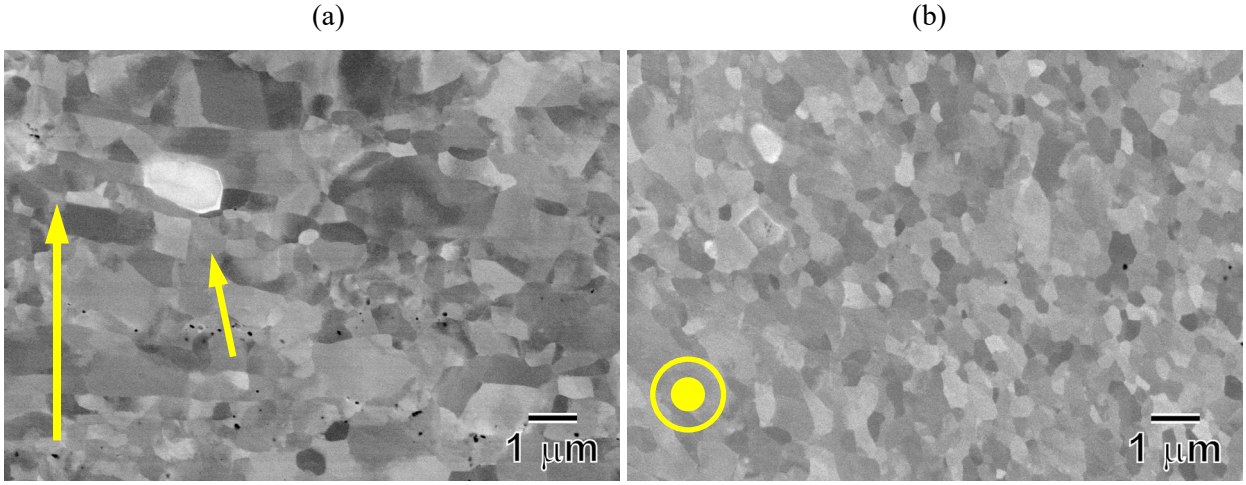

Figure 16. SEM-BSE micrographs obtained at higher magnification of the microstructure present in the OFRAC alloy after annealing at 1150ºC for 8 h in the (a) LT orientation and (b) TS orientation. The yellow arrow and dot represent the extrusion direction.

map that correponds to grain misorientations measuring <15º (Fig. 17d). The regions consisting of the small grains are associated with much larger grain misorientation angles. The average grain diameter determined from grain area measurements using the EBSD software was 380 +/- 780 nm. The same reasoning mentioned previously is responsible for the large standard deviation in the average grain size. The much larger standard deviation over the average grain size indicates that more grain coarsening occurred during the 1150 ºC annealing. Abnormal grain growth mechanisms may have contributed to the large grains that contained sub-structures.

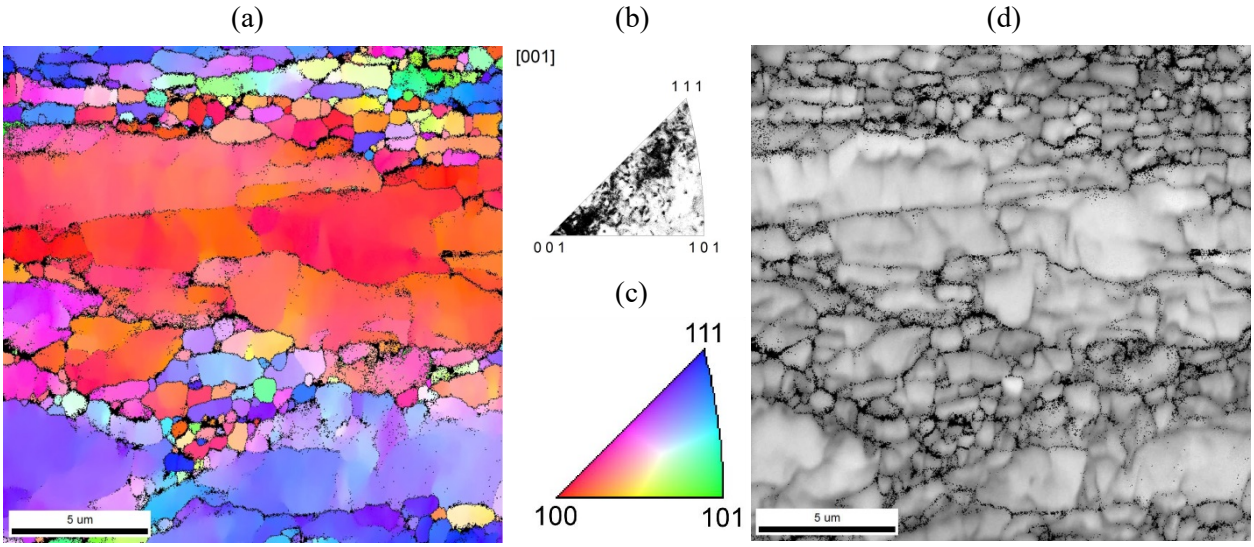

Figure 17. (a) EBSD pole figure map of the annealed 1150ºC/8 h OFRAC alloy in the LT orientation, (b) inverse pole figure of the grains in the [001] normal direction, (c) the color triangle associated with the orientation of the grains observed in the EBSD pole figure map and (d) the grain boundary map showing the misorientation angles between the grains.

Figure 18 shows the results obtained by LEAP analysis of the specimen prepared from the annnealed 1150ºC/8h OFRAC alloy. The reconstructed element maps show the spatial distributions of Y (Fig. 18a), Ti (Fig. 18b), O (Fig. 18c), Nb (Fig. 18d) amd C (Fig. 18e). The element maps show a high concentration of uniformly distributed Ti-Y-O enriched nano-size oxide (nanoclusters) particles in all the specimens. The element maps for Nb and C indicate that they are also associated with the nanoclusters. However, it is not possible from the element maps to determine if Nb and C are associated with the structure of the nanocluster or have segreated to the surface. The corrected average diameter and number density of the Ti-Y-O enriched nanoclusters was 4.00 nm and 2.3×10^{23} m^{-3}, which indicates that some coarsening of the nanoclusters occurred.

The composition and size correlation of the analyzed nanoclusters is shown in the Y-Ti-O ternary diagram in Figure 19. The diameter of the circle indicates the size of the analyzed nanocluster in this figure. The composition of the nanoclusters showed a shift in the Ti, Y and O concentrations primarily towards the equilibrium $Y_2Ti_2O_7$ pyrochlore phase with some association with the Y_2TiO_5 phase. The composition spread in the APT data also decreased. Both of these results were due to the high temperature annealing conditions of 8h at 1150ºC, which most likely influcence long range diffusional processes that led to the composition changes and size increase of the nanoclusters. However, even at 4 nm, the nanoclusters have not undergone significant coarsening that indicates these particles show remarkable thermal stability.

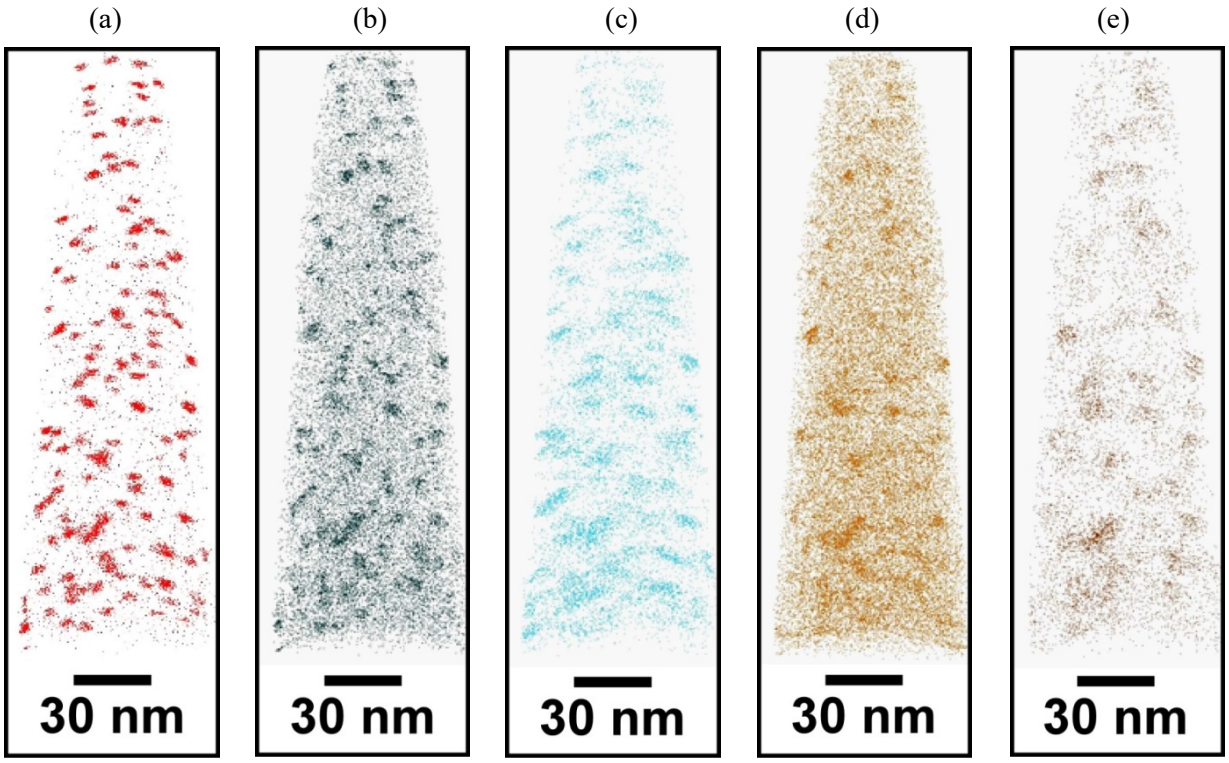

Figure 18. LEAP analysis of the specimen prepared from the annealed 1150ºC+8h OFRAC alloy showing element maps of (a) Y, (b) Ti, (c) O, (d) Nb and (e) C.

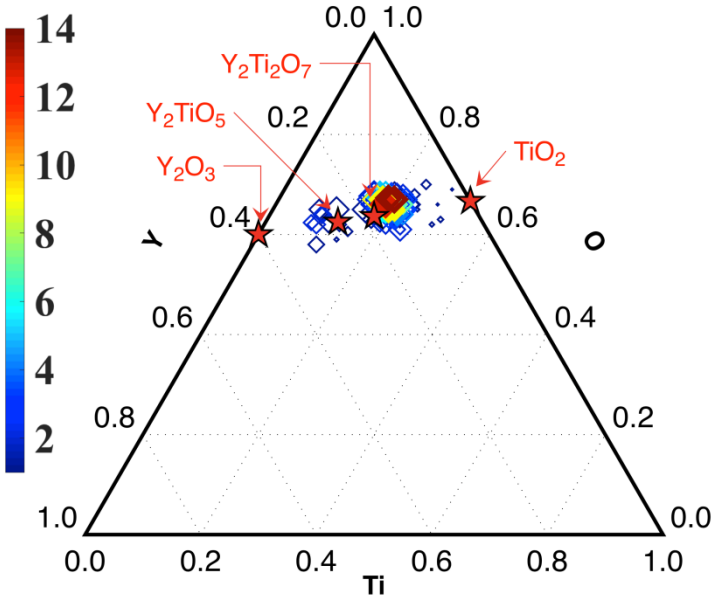

Figure 19. The Y-Ti-O ternnary diagram obtained from the LEAP analysis of the specimen prepared from the annealed 1150ºC+8h OFRAC alloy showing the composition and size (circle diameter) of the analyzed nanoclusters.

4. HIGH-TEMPERATURE MECHANICAL PROPERTEIS

The tensile properties of OFRAC were obtained in the as-extruded condition and after annealing for 8h at 1050ºC and 1150ºC. The tensile tests were conducted on an MTS servo-hydraulic uniaxial load frame using SS-3 miniature sheet tensile specimens (overall length of 25 mm with gage dimensions of 7.62 mm long × 1.524 mm wide × 0.762 mm thick) from room temperature (25ºC) to 800ºC in air using a strain rate of 10^{-3} s^{-1}.

The thermal creep properties of OFRAC were determined using the strain-rate jump (SRJ) method. These tests were conducted on an MTS servo-hydraulic uniaxial load frame in displacement control mode using SS-3 tensile specimens fabricated from the OFRAC bar in the as-extruded condition. The SRJ tests were performed in air at 550ºC, 600ºC, 700ºC and 800ºC by increasing the strain rate by one order of magnitude for each SRJ test, with strain rate sensitivity examined over a total of four orders of magnitude. The SRJ tests started at 1.5×10^{-7} s^{-1} and ended at 1.5×10^{-3} s^{-1}; each SRJ test ended when the stress no longer changed with time.

4.1 Tensile tests

Figure 20 shows the stress-strain curves for the extruded OFRAC condition from 25ºC to 800ºC. The results show a balance of high strength and good ductility over the temperature range. Although high work hardening was not observed after yielding, the OFRAC alloy exhibited good ductility at all test temperatures, including at room temperature where the yield and ultimate strength exceeded 1.2 GPa with uniform elongation exceeding 9%.

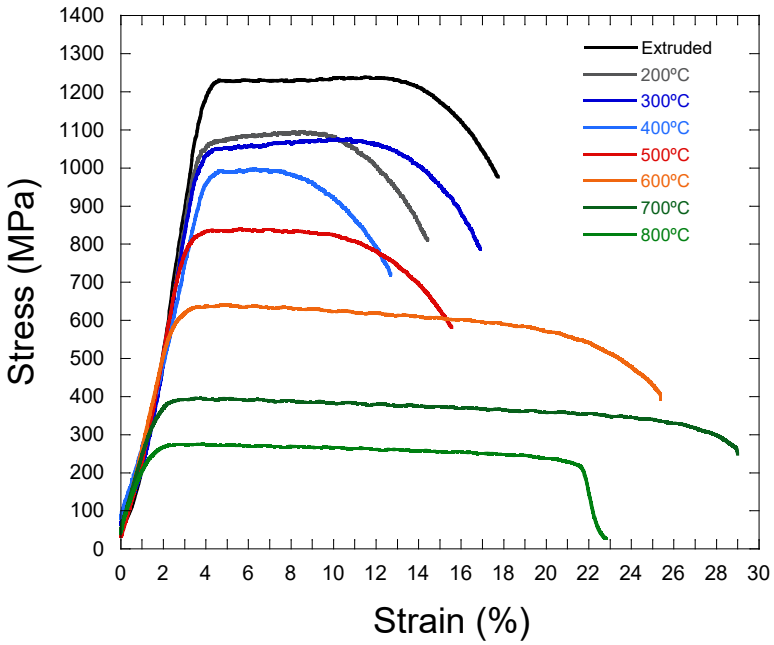

Figure 20. Stress-strain curves over the temperature range from 25ºC to 800ºC.

Figure 21 shows the tensile properties of OFRAC in the extruded and annealed conditions from 25ºC to 800ºC. Although the yield stress (YS) decreases after the 1150ºC annealing (e.g. by ~100 MPa at room temperature), there are only minor variations in ultimate tensile strength (UTS) between the extruded and annealed specimens over the 20-800ºC tensile test temperature range. Plus, the YS values for the annealed and extruded conditions converge at 600ºC to 800ºC. The annealing treatments influenced ductility in a more complicated manner. In general, the uniform elongation (UE) was decreased above ~200ºC while the total elongation (TE) was increased at most of the test temperatures. Overall, the tensile results on the high

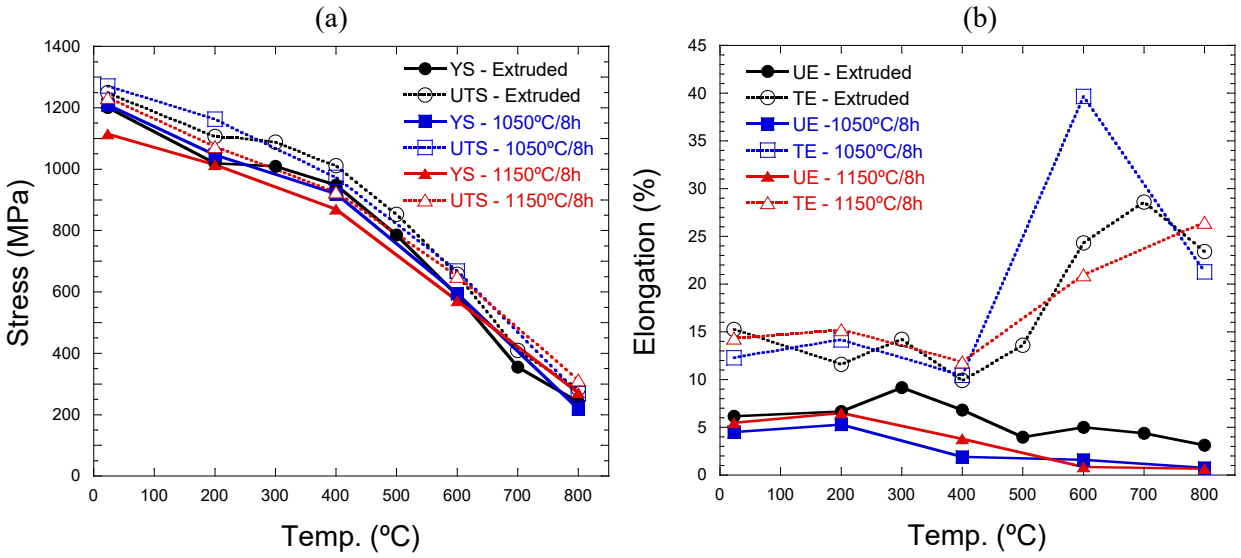

Figure 21. High-temperature stability of the tensile properties. (a) strength and (b) ductility.

4.2 Strain-rate jump creep tests

temperature annealed specimens suggest that tensile properties derived from the microstructure of OFRAC in the extruded condition were resistant to property deterioration for annealing conditions as high as 1150ºC (~0.76 T_M, where T_M is the absolute melting temperature).

4.2 Strain rate jump tests

Figure 22 shows the type of results that were obtained from the strain-rate jump tests conducted on the SS-3 specimens of OFRAC in the extruded condition. Starting at the lowest strain rate of 1.5×10^{-7} s^{-1} at the test temperature (550ºC, 600ºC, 700ºC and 800ºC), the specimen is deformed by applying a constant strain rate that causes the flow stress to increase until it reaches a steady-state and does not change with time. The strain rate is then increased by one order of magnitude until the flow stress reaches the next steady state.

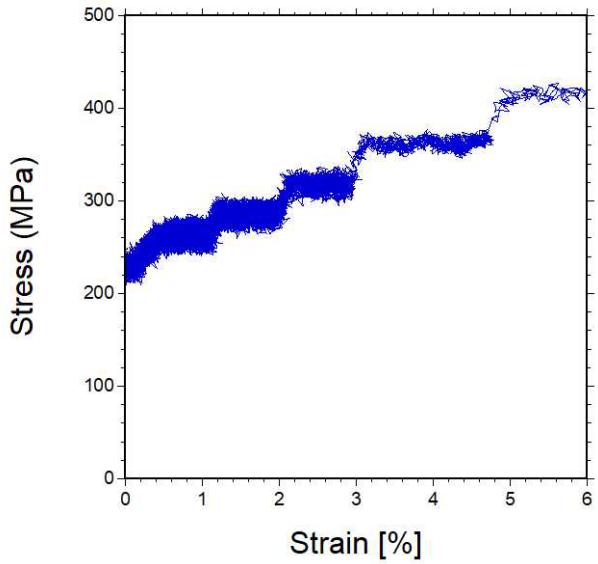

Figure 22. Plot showing the strain rate jump test that was performed at 700ºC.

This procedure is continued until the strain rate changes cover four orders of magnitude. From Figure 22, the results show the stress increases with increasing strain rate, which reflects the positive strain rate dependence that is characteristic of bcc metals, such as Fe.

The results of the SRJ tests conducted on the SS-3 specimens of OFRAC at 550ºC, 600ºC, 700ºC and 800ºC are shown in Figure 23. The SRJ data is plotted with the log of the measured stress as a function of the strain rates. With this type of data, the stress exponent (n) can be determined from the following relationship:

$$n = \left(\frac{\log \dot{\varepsilon}_m}{\log \sigma} \right)$$

and is determined by plotting the values of the log minimum creep rate ($\dot{\varepsilon}_m$), or strain rate from the SRJ test, against log stress (σ) and measuring the slope from the exponential line fit. The results showed high values of n at all test temperatures.

Figure 23 also shows the stress exponent values obtained by load-to-failure creep tests for HT-9 F/M steel [9] and three austenitic stainless steels [10,11]. The calculated stress exponent values for OFRAC and those obtained for HT-9 and the stainless steels are shown in the legends of Figure 23 and are plotted as a function of test temperature in Figure 24.

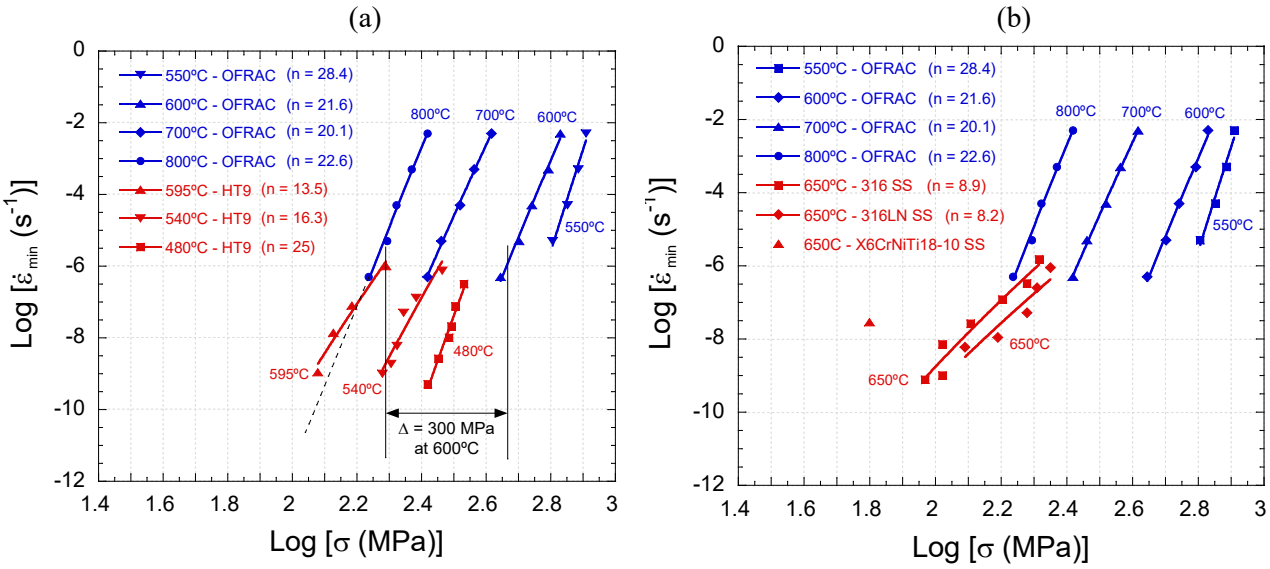

Figure 23. Comparison of thermal creep behavior of OFRAC (determined from SRJ tests) with (a) HT-9 [9] and (b) three austenitic stainless steels [10,11]. The calculated stress exponent (n) is shown for each set of creep data.

The results show higher creep stress exponents for OFRAC over the temperature range of 550ºC to 800ºC than those for HT-9 at lower test temperatures. The stress exponent value (n=25) for HT-9 at 480ºC (Fig. 23a) was similar to the values for OFRAC, which were obtained at much higher temperatures. Furthermore, the stress required to cause similar creep rates at the test temperatures was significantly higher in OFRAC than HT-9. As shown in Figure 23a, the stress to induce a strain rate of ~10^{-6} s^{-1} at ~600ºC for OFRAC was ~300 MPa higher compared to HT-9 (500 vs. 200 MPa) that was tested at a similar temperature of 595ºC. For a similar creep rate of 10^{-7} s^{-1} at 150 MPa, the test temperature for OFRAC was 800ºC compared to 595ºC for HT-9. These results imply that the operating temperature limit for OFRAC will be ~150-200ºC higher compared to HT-9.

The thermal creep performance of OFRAC was also superior to that of 316 and 316LN austenitic stainless steels (Fig. 23b). The results show the stainless steels possessed a creep rate of 10^{-6} s^{-1} at 650ºC with applied stresses of 200-250 MPa. For the SRJ tests for OFRAC, test temperatures at 700ºC and 800ºC resulted in a similar strain rate for stresses of 250 MPa and 150 MPa, respectively. The stress exponent values for 316 SS and 316LN SS at 650ºC were a factor of two to three lower than that of OFRAC (Fig. 24), which indicates that a different creep mechanism such as diffusional creep is occurring in the stainless steels compared to that in OFRAC. It is expected that the oxide dispersion present in OFRAC will lead to dislocation (power law) creep mechanisms even up to 800ºC based on the high stress exponent values.

The high dependence of minimum creep rate with changes in stress indicates that quite low creep rates will occur for OFRAC at higher temperatures and stresses compared to HT-9 and stainless steel. However, longer term (>>10,000 h) thermal creep testing of OFRAC will be required to confirm the short-term SRJ predictions.

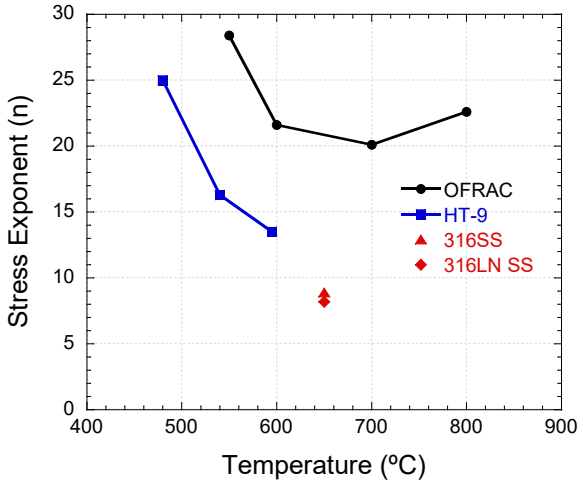

Figure 24. The temperature dependent values of stress exponents for OFRAC, HT-9, 316SS and two 316 stainless steels.

5. SUMMARY

The new nanostructured ferritic alloy, OFRAC, was developed for the advanced sodium fast reactor cladding and core internals. Leveraging experience obtained on mechanical alloying in development of the NFA 14YWT, the composition and microstructure of OFRAC was tailored to meet strength as well as creep and swelling resistance requirements where historic austenitic and ferritic SFR cladding materials are not suitable. The highlights of the microstructure characterization studies revealed a uniform dispersion of a high concentration of Y-Ti-O enriched oxide particles, or nanoclusters, and that Nb along with excess Ti were very effective in sequestering interstitial C and N that are commonly introduced as contamination during ball milling of powder. The removal of these interstitial elements from the bcc-Fe matrix of OFRAC should be beneficial to plastic deformation during extreme fabrication into complex components such as thin wall tubing. The results of the tensile tests showed an excellent balance in strength and ductility from room temperature to 800ºC. The thermal creep resistance at elevated temperatures and stresses obtained was obtained from strain rate jump testing showed that OFRAC possessed high stress exponents at high stresses and temperatures of 550ºC, 600ºC, 700ºC and 800ºC. This thermal dependence of minimum creep rate indicates that OFRAC will show quite low creep rates at higher temperatures and stresses compared to HT-9 and stainless steel. While the irradiation behavior of OFRAC to high dose is currently ongoing, based

on the current state of knowledge regarding radiation damage processes exhibited with 14YWT, the OFRAC alloy is expected to exhibit excellent swelling and irradiation creep resistance.

6. REFERENCES

[1] D.T Hoelzer, C.P. Massey, S.J. Zinkle, D.C. Crawford and K.A. Terrani, Submitted to Journal of Nuclear Materials, Reference: JNM_2019_720, June 17, 2019.

[2] S.H. Kim, W.S. Ryu and I.H. Kuk, Journal of the Korean Nuclear Society, 31(6), 1999, 561-571.

[3] J.J. Hoon, Doctor of Philosophy: "The Effect of Mo or W on TiC Coarsening in HSLA Steel," Pohang Univeristy of Science and Technology, 2012.

[4] E.V. Morales, ed., Book: "Alloy Steel - Properties and Use," InTech, 2011.

[5] L.Dai, Q. Guo, Y. Liu, L. Yu and H. Li, Materials Science & Engineering A., 674 2016, 579-587.

[6] M.K. Miller, D.T. Hoelzer, E.A. Kenik and K.F. Russell, Intermetallics, 13, 2005, 387-392.

[7] M.K. Miller, D.T. Hoelzer, E.A. Kenik and K.F. Russell, Journal of Nuclear Matearials, 329-333, 2004, 338-341.

[8] C.P. Massey, D.T. Hoelzer, R.L. Seibert, P.D. Edmondson, A. Kini, B. Gault, K.A. Terrani, and S.J. Zinkle, Journal of Nuclear Materials, 522, 2019, 111-122.

[9] H.J. Ryu, Y.S. Kim, A.M. Yacout, Thermal creep modeling of HT9 steel for fast reactor applications, Journal of Nuclear Materials, 409, (2011), 207–213.

[10] G. Sasikala, S.L. Mannan, M.D. Mathew, K.B. Rao, Creep deformation and fracture behavior of types 316 and 316L (N) stainless steels and their weld metals, Metallurgical and Materials Transactions A, 31, (2000), 1175–1185.

[11] J. Brnic, G. Turkalj, M. Canadija, D. Lanc, S. Krscanski, M. Brcic, Q. Li, J. Niu, Mechanical Properties, Short Time Creep, and Fatigue of an Austenitic Steel, Materials (Basel). 9, (2016), 298.